The DOI for this manuscript is doi: 10.1175/JTECH-D-18-0168.1

Merckelbach, L., A. Berger, G. Krahmann, M. Dengler, and J. Carpenter, 2019: A dynamic flight model for Slocum gliders and implications for turbulence microstructure measurements. J. Atmos. Oceanic Technol. doi:10.1175/JTECH-D-18-0168.1, in press.

A dynamic flight model for Slocum gliders and implications for turbulence microstructure measurements

Lucas Merckelbach* and Anja Berger

Institute of Coastal Research, Helmholtz-Zentrum Geesthacht, Geesthacht, Germany

Gerd Krahmann and Marcus Dengler

GEOMAR Helmholtz Centre for Ocean Research Kiel, Kiel, Germany

Jeffrey R. Carpenter

Institute of Coastal Research, Helmholtz-Zentrum Geesthacht, Geesthacht, Germany

* *Corresponding author address:* Lucas Merckelbach, Institute of Coastal Research, Helmholtz-Zentrum Geesthacht, Max-Planck-Straße 1, 21502 Geesthacht, Germany

E-mail: lucas.merckelbach@hzg.de

ABSTRACT

The turbulent dissipation rate ε is a key parameter to many oceanographic processes. Recently gliders have been increasingly used as a carrier for microstructure sensors. Compared to conventional ship-based methods, glider-based microstructure observations allow for long duration measurements under adverse weather conditions, and at lower costs. The incident water velocity U is an input parameter for the calculation of the dissipation rate. Since U can not be measured using the standard glider sensor setup, the parameter is normally computed from a steady-state glider flight model. As ε scales with U^2 or U^4, depending whether it is computed from temperature or shear microstructure, flight model errors can introduce a significant bias. This study is the first to use measurements of in-situ glider flight, obtained with a profiling Doppler velocity log and an electromagnetic current meter, to test and calibrate a flight model, extended to include inertial terms. Compared to a previously suggested flight model, the calibrated model removes a bias of approximately 1 cm s^{-1} in the incident water velocity, which translates to roughly a factor of 1.2 in estimates of the dissipation rate. The results further indicate that 90% of the estimates of the dissipation rate from the calibrated model are within a factor of 1.1 and 1.2 for measurements derived from microstructure temperature sensors and shear probes, respectively. We further outline the range of applicability of the flight model.

1. Introduction

The dissipation rate of turbulent kinetic energy is a parameter that plays a key role in many physical and biogeochemical processes in oceans and coastal seas. However, direct oceanic measurements of turbulence are relatively scarce, as most observations stem from free-falling profilers, operated from seagoing vessels. The monetary and labor cost of taking such profiles is therefore substantial, and is most often limited to relatively calm conditions.

An emerging alternative to ship-based profiling is the use of ocean gliders, a class of buoyancy-driven autonomous underwater vehicles (Davis et al. 2002; Rudnick 2016). Although gliders have been increasingly used over almost two decades, it is only recently that turbulence profilers have been mounted onto gliders (Wolk et al. 2009; Fer et al. 2014; Peterson and Fer 2014; Palmer et al. 2015; Schultze et al. 2017; St. Laurent and Merrifield 2017; Scheifele et al. 2018). The glider as measurement platform has relatively low levels of vibration and mechanical noise, mainly due to the absence of a propeller. This makes gliders suitable for turbulence observations using shear probes. Using gliders as an alternative to ocean-going ships removes a substantial part of the human factor in the data collection process, and therefore eases long duration data collection, while reducing costs, and effectively removes any measurement constraints imposed by adverse weather conditions.

Despite the advantages of glider-based turbulence measurements, the major drawback of this setup is the uncertainty in the flight of the glider. A required parameter in the processing of microstructure shear and temperature measurements is the speed of flow past the sensors. The speed through water enters the processing raised to the fourth power when using airfoil shear probes, and to the second power when using micro-temperature sensors (see Sec. 6a for details). For free-falling vertical profilers, this is usually determined from the rate of change of pressure.

For glider-based measurements, this only gives the vertical speed of the glider, with a horizontal speed that must be either measured directly, or modelled.

It is uncommon for a microstructure glider to be equipped with a device that directly measures (a horizontal component of) the speed through water, so that often a flight model is used for the computation of turbulent dissipation (Fer et al. 2014; Peterson and Fer 2014; Palmer et al. 2015; Schultze et al. 2017; St. Laurent and Merrifield 2017; Scheifele et al. 2018).

The most commonly used flight model is that of Merckelbach et al. (2010), who assume a steady-state balance between buoyancy, drag and lift, and use the measured pitch angle and buoyancy change achieved by the buoyancy engine, to compute the speed through water (Fer et al. 2014; Peterson and Fer 2014; Palmer et al. 2015; Schultze et al. 2017; Scheifele et al. 2018). The numerical evaluation of these forces requires values to be attributed to a number of coefficients, such as the glider density, compressibility, drag and lift coefficients. Merckelbach et al. (2010) show that the glider density, compressibility, and drag coefficients can be determined from standard glider sensors, however, they note that it is not possible to simultaneously determine the lift coefficient without a direct measurement of the horizontal component of the glider speed.[1] The model therefore relies on tabulated coefficients from aerodynamic studies of bodies of similar shape in its specification of lift coefficients. To date, no study has been published where the glider flight model by Merckelbach et al. (2010) is calibrated and compared with direct measurements of the glider velocity through water.

In summary, glider-based turbulence microstructure measurements represent new possibilities for sampling ocean turbulence, but suffer from uncertainties in glider flight models which are par-

[1]Depth-averaged velocities computed using surface GPS data, as attempted by Merckelbach et al. (2010), would provide such a measurement. However, for calibrating the lift coefficient, water velocities along the track of the glider must be known with a bias of less than approximately 1 cm s^{-1}, making this method unreliable.

ticularly sensitive, and as yet untested. In this work, a Teledyne WebbResearch Slocum Electric Shallow glider has been fitted with a Teledyne RDI Explorer Doppler Velocity Log (DVL). This device primarily measures the horizontal and vertical components of the glider velocity with respect to the sea bed (bottom track), provided the seabed is within the acoustic range of about 80 m. A profiling mode also allows the measurement of the glider velocity relative to the water at some distance below the glider (about 5-15 m). In addition, we also utilise data collected from an electromagnetic current meter mounted inside a microstructure package to assess glider flight characteristics. Using these data we calibrate and extend the glider flight model of Merckelbach et al. (2010) based on direct measurements of glider flight, as well as examine the implications for the accuracy of turbulent dissipation rate estimates as measured with glider-mounted microstructure sensors.

2. Background: steady-state glider flight model

Key to the work presented herein is a steady-state planar glider flight model developed by Merckelbach et al. (2010) in order to obtain vertical water velocities from glider observations. The model is based on a horizontal (x) and vertical (z) force balance, in which the acceleration terms are neglected, given by [2]

$$0 = \sin(\theta+\alpha)F_{\mathrm{L}} - \cos(\theta+\alpha)F_{\mathrm{D}} \tag{1}$$

$$0 = F_{\mathrm{B}} - F_{\mathrm{g}} - \cos(\theta+\alpha)F_{\mathrm{L}} - \sin(\theta+\alpha)F_{\mathrm{D}}, \tag{2}$$

[2]This system of equations is identical to the equations given by Merckelbach et al. (2010), if their equations are corrected for an unfortunate sign error.

where the pitch angle θ and the angle of attack α are defined in Figure 1. The forces that act on the glider are due to buoyancy F_{B}, gravity F_{g}, lift F_{L} and drag F_{D}:

$$F_{\mathrm{g}} = m_{\mathrm{g}} g, \tag{3}$$

$$F_{\mathrm{B}} = g\rho \left(V_{\mathrm{g}}(1 - \varepsilon_{\mathrm{c}} P + \alpha_T (T - T_0)) + \Delta V_{\mathrm{bp}} \right), \tag{4}$$

$$F_{\mathrm{D}} = \frac{1}{2} \rho S U^2 \left(C_{\mathrm{D}_0} + \alpha^2 C_{\mathrm{D}_1} \right), \tag{5}$$

$$F_{\mathrm{L}} = \frac{1}{2} \rho S U^2 C_{\mathrm{L}}(\alpha), \tag{6}$$

$$C_{\mathrm{L}}(\alpha) = a\alpha, \tag{7}$$

where m_{g} is the mass of the glider, g the acceleration due to gravity, ρ the in-situ density, V_{g} the volume of the glider at atmospheric pressure, ε_{c} the coefficient of compressibility, α_T, the thermal expansion coefficient of the glider, ΔV_{bp} the volume change achieved by the buoyancy engine, S the total surface area of the wings, U the magnitude of the glider speed through water, and C_{D_0} and C_{D_1} the parasite and induced drag coefficients, respectively. For small angles of attack α, the lift coefficient C_{L} is assumed to be linear in the angle of attack, proportional to the lift angle coefficient a.

An expression for U can be obtained by either eliminating F_{D} or F_{L} from (1) and (2), and substituting from (5) and (6), respectively, relating U to either drag coefficients, or lift angle coefficients. Expressed in drag coefficients, we get

$$\sin(\theta + \alpha)(F_{\mathrm{B}} - F_{\mathrm{g}}) - \frac{1}{2} \rho S U^2 (C_{\mathrm{D}_0} + C_{\mathrm{D}_1} \alpha^2) = 0. \tag{8}$$

In addition, an expression for the angle of attack is found by combining (1), and (5)–(7), yielding

$$\alpha = \frac{C_{\mathrm{D}_0} + \alpha^2 C_{\mathrm{D}_1}}{a \tan(\theta + \alpha)}. \tag{9}$$

Equations (8) and (9) provide a model to compute the steady state flight condition at any time, given measurements of the buoyancy drive, pitch angle, and in-situ density, and a set of model coefficients for drag, lift, compressibility and thermal expansion (if applicable).

Merckelbach et al. (2010) determine model coefficients by minimising a cost-function that is mathematically identical to

$$R_0 = \frac{1}{N}\sum_{i=0}^{N-1}\left[U[i]\sin(\theta[i]+\alpha[i]) + \frac{\mathrm{d}h}{\mathrm{d}t}[i]\right]^2. \tag{10}$$

Herein, the depth-rate $\mathrm{d}h/\mathrm{d}t$ and pitch θ are observations with index i from a total of N values, and U and α are the corresponding model results using (8) and (9). It can be shown, however, that the cost-function does not yield unique values if both the parasite drag and the lift angle coefficient are present in the minimisation parameter space. Although the model may be optimised for the vertical velocity component, the horizontal velocity component, and therefore, the speed through water, depends on the actual value of the lift angle coefficient. This means that depth-rate observations alone are not sufficient to calibrate a glider flight model that also computes accurately the glider speed through water. Consequently, additional measurements of a non-vertical glider velocity component are required, and are presented in Section 4.

3. Dynamic glider flight model

Although the steady-state glider flight assumption seems reasonable for most practical situations, a dynamic, non-steady-state glider flight model may provide a better estimate of the glider speed for rapidly changing conditions, for example when strong density gradients are present or around dive-to-climb turning points. Requiring little additional effort, such a dynamic flight model can be obtained by (re-)inserting the acceleration terms into the steady-state model. Besides the glider mass accounting for its inertia, also the so-called *added mass* needs to be considered. Added

mass terms arise from the fact that if a submerged body accelerates, not only does the body's mass oppose the acceleration, also the flow around the body changes. From an energy principle it then follows, that the body does work on the ambient water mass and additional forces act on the submerged body (Imlay 1961). These additional forces can be conveniently written as a 6x6 mass matrix, multiplied by a vector composed of three linear and three angular acceleration components (Newman 1977).

For planar flight with negligible rotational accelerations, which are typical for glider flight, the inertial forces to be inserted into the dimensional steady-state model can be simplified to $\mathbf{M}\begin{bmatrix} \mathrm{d}u/\mathrm{d}t & \mathrm{d}w/\mathrm{d}t \end{bmatrix}^T$. Herein u and w are the horizonal and vertical glider velocity components in a georeferenced coordinate system, and $\mathbf{M}$ is a 2x2 matrix, composed of the glider mass on the diagonal, $m_\mathrm{g}\mathbf{I}$, where $\mathbf{I}$ is the identity matrix, and a 2x2 matrix $\mathbf{m}$, representing the added mass terms. When expressed in the orthogonal glider referenced coordinate system, (ξ,η) (see Figure 1), with its axes (from the glider's perspective) pointing forward and upward, the added mass matrix $\mathbf{m}$ for a glider shaped object can adequately be described by a diagonal matrix, $\mathrm{diag}(m_{11},m_{22})$, where m_{11} and m_{22} are the dominant added mass components (Imlay 1961; Newman 1977). Expressed in the (x,y) coordinate system, the transformed $\mathbf{m}$ is not necessarily diagonal, and the inertia matrix becomes

$$\mathbf{M} = m_\mathrm{g}\mathbf{I} + \begin{bmatrix} m_{11}\cos^2(\theta) + m_{22}\sin^2(\theta) & (m_{11}-m_{22})\cos(\theta)\sin(\theta) \\ (m_{11}-m_{22})\cos(\theta)\sin(\theta) & m_\mathrm{g} + m_{22}\cos^2(\theta) + m_{11}\sin^2(\theta) \end{bmatrix}. \tag{11}$$

Based on the expressions given in Imlay (1961) for a finned prolate spheroid shaped glider with a length of 2 m, the numerical values of the added mass terms are estimated at $m_{11} = 0.2 \cdot m_\mathrm{g}$ and $m_{22} = 0.92 \cdot m_\mathrm{g}$.

With this result, the dynamic flight model can be written as [see (1), (2)]

$$\mathbf{M}\frac{\mathrm{d}}{\mathrm{d}t}\begin{bmatrix} u \\ w \end{bmatrix} = \begin{bmatrix} \sin(\theta+\alpha)F_{\mathrm{L}} - \cos(\theta+\alpha)F_{\mathrm{D}} \\ F_{\mathrm{B}} - F_{\mathrm{g}} - \cos(\theta+\alpha)F_{\mathrm{L}} - \sin(\theta+\alpha)F_{\mathrm{D}} \end{bmatrix}. \tag{12}$$

To integrate this initial value problem using a classical Runge-Kutta (RK4) explicit method, we specify $u = w = 0$ as initial conditions, and when the glider is at the surface. Furthermore, the incident flow velocity is set equal to $U = \sqrt{u^2 + w^2}$. In fact, this is true only if the water column behaves as a steady-state flow without shear. However, under most conditions the oceanic shear is small so that the errors of the estimated lift and drag forces can be assumed small too. We also note that transient effects due to changing flow conditions on the drag and lift forces generated, are not accounted for. Both the steady-state and dynamic models are implemented in Python 3. The source code, documentation and examples are available at a public repository under the MIT software license (Merckelbach 2018).

4. Experimental data

a. Instrumentation

The glider COMET is a Teledyne Webb Research G2 shallow electric glider, equipped with a Seabird GP-CTD, a Rockland Scientific Microrider, and a profiling Teledyne RDI 600 kHz phased array Explorer DVL (Doppler Velocity Log). The CTD received a firmware update allowing it to sample at 1 Hz, rather than the default 0.5 Hz. A thermal lag correction algorithm, similar to that described by Garau et al. (2011) was applied to correct the measured conductivity within the conductivity cell. The Microrider sampled pressure and pitch at 64 Hz.

The DVL mounted on glider COMET measured velocities acoustically along four beams in Janus configuration at a 30° angle. The device was mounted in a separate hull section, placed in front of the science bay (Figure 1). Since the DVL is primarily designed to measure bottom track

velocities, it was installed downward-looking, and mounted with a forward pitch angle of 11°. The mounting angle ensures that if the glider is at a nominal dive angle of 26°, the principal axis of the tetrahedron defined by three of its beams is aligned with the vertical ordinate.

Besides measuring bottom track velocities, the DVL was configured (by means of a firmware upgrade) to collect three-dimensional current profiles, like a classical acoustic Doppler current profiler (ADCP). The DVL was set up to continuously record ensembles, each consisting of 10 profile pings with a bin size of 2 m, and 2 bottom track pings. With a typical ping rate of 7 Hz (see the instrument's datasheet (TeledyneRDI 2017)) the measurement time of an ensemble amounted to up to 1 second, during which the vertical distance travelled by the glider was about 10-15 cm. The realised sample rate of the ensembles was between once per 4 and 3 seconds, indicating a significant amount of time required to process and store the ensemble data.

According to the DVL's datasheet, the standard deviations for single bottom track and velocity profile pings are 1.0 and 4.7 cm s^{-1}, respectively. For the configuration used, the standard deviation of the profile velocity relative to the sea bed, computed from an ensemble amounts, to 1.7 cm s^{-1}, assuming that all pings can be treated as independent variables. As this is calculated for ideal conditions, we use a more conservative value, estimated at $\sigma = 2.5$ cm s^{-1}, allowing for additional uncertainty due to vertical shear, horizontal heterogeneity of the flow, and pitch, heading and roll readings.

The DLV measurements are georeferenced using the pressure measured by the glider, after correcting for a small delay of about 3 seconds in DVL measurements. The time delay was computed for each profile by matching the glider and DVL time stamps of the pitch, a parameter that is measured by the glider's attitude sensor and fed into the DVL.

Raw DVL data were subjected to a number of quality checking algorithms to mask low quality data, as well as data correction algorithms. Following Todd et al. (2017), a pipeline of operations

was set up to correct the speed of sound using the salinity measured by the glider; correct for offsets in roll and pitch; mask relative water velocities and bottom track velocities that exceed 0.75 m s^{-1}; mask velocities for which the signal-to-noise ratio (SNR) is smaller than 3, where $\mathrm{SNR} = 10^{(S_{\mathrm{dB}} - N_{\mathrm{dB}})/10}$ with S_{dB} and N_{dB} the signal and noise levels in dB; and finally, mask velocities the signal levels of which exceed 75 dB. It is noted that in this work the SNR threshold was set more permissively to 3, rather than 20 as used in Todd et al. (2017).

In order to compute eastward, northward and upward velocity components, the DVL uses heading, pitch and roll angles that are reported by the glider. It was found that the difference between the upward bottom track velocity and the depth-rate was positively biased for up casts and negatively biased for down casts. It turned out that the tilt sensor had leaked a small amount of electrolyte fluid, so that pitch and roll angles were reported larger than they were in reality. The associated error in the pitch and roll angles is proportional to their real values (Pheiffer, pers. comm.). Matching upward bottom track velocity and depth-rate yielded a scaling factor of 0.83. Prior to the step to correct the pitch and roll offsets in the processing pipeline, the DVL velocities were recomputed using scaled pitch and roll angles.

The glider IFM03 is a Teledyne WebbResearch G1 deep glider (short version) equipped with an unpumped Seabird CTD and a Rockland Scientific Microrider (similar to the one mounted on top of the glider COMET). Added to this Microrider (by Rockland Scientific) was an electromagnetic current (EMC) sensor (AEM1-G, by JFE Advantech Co. LTD). CTD data were recorded at a sample rate of 1 Hz, and were corrected for thermal lag effects following Garau et al. (2011). The relevant Microrider data (pitch, pressure and EMC velocity) were logged at a rate of 64 Hz.

The EMC sensor measures the axial speed of the glider through the water. The sensor was calibrated in a water tank by the manufacturer JFE Advantech. This was done by towing the EMC sensor mounted to a MicroRider hull at different speeds through the tank. Although the EMC

sensor is sampled at 64 Hz, the sensor itself has a measurement frequency of 15 Hz. During the post-processing the velocity measurements were averaged to yield a time series with a frequency of 1 Hz, with each sample being the average of about 10 – 15 individual measurements. The accuracy of the velocity measurements claimed by the manufacturer is 0.5 cm s^{-1} or 2% of the readings[3], without stating the measurement bandwidth. It is therefore not clear how much averaging of raw data samples is required to obtain this accuracy. We assume, that the uncertainty in the EMC readings is 1 cm s^{-1} or better for the velocity data averaged to 1 Hz time series.

b. Datasets

For the analysis of the glider flight model three datasets were selected (see Table 1 for a summary). Dataset I was selected, because the data of glider COMET include water velocity measurements measured with a DVL. Importantly, the water depth was shallow enough ($\approx$ 60 m) for the DVL to record bottom track velocities during the glider's down casts, which is essential to compute relative glider velocities (Section 4c). Due to the presence of a strong halocline, the dives were limited to depths of 40 m. The glider was flown with pitch angles set to $\pm 26^{\circ}$.

Dataset III was selected, because IFM03 carried a Microrider that was retrofitted with an EMC, the measurement principle of which is entirely different than the DVL. In contrast to dataset I, this dataset also contains reliable velocity measurements on the up casts, as well as during the transitions from dive to climb. This glider was programmed to dive to 800 m, or when limited by topography, to 15 m above the sea bed. From this dataset, we selected a sequence of profiles where the glider dives to the full 800 m. The glider was flown with fixed battery positions resulting in typical down cast and up cast pitch angles of 32° and 28°, respectively.

[3] https://rocklandscientific.com/wp-content/uploads/2017/05/RSI-Data-Sheet-MicroPodEM-A4-1_00-web.pdf

Dataset II used the same glider setup as dataset I, however, the glider was flown in water depths that were too large to obtain bottom track velocities for most of the profiles. Hence, the DVL data from this dataset are not used. This dataset is still of interest, because the day prior to recovery was used to fly the glider for short periods at two different pitch angles than the standard 26°, namely $\pm 20°$, and $\pm 30°$, in order to quantify the effects of the induced drag.

c. Relative glider velocities from DVL measurements

The velocity profile data, configured to be outputted by the DVL as eastward, northward and upward velocity components, represent the water velocity relative to the glider. The first bin is found at 2.92 m from the transducer. However, the data from the first two bins often show a signal that is distinctively different from the other bins and therefore the first two bins are excluded from the analysis to follow. The echos from bins positioned further away than about 15 m were often weak, not yielding a signal with a sufficiently high signal-to-noise ratio. As a result, the typical range for which meaningful data were obtained is some 7 to 15 m away from the glider. In the presence of significant vertical shear, the relative velocity of the glider measured by the DVL from a particular depth may not represent the actual relative velocity at the depth of the glider. In order to improve the estimates of the relative water velocity at the glider's position, we used the following approach.

Consider a glider collecting data using a downward-looking DVL while diving (Figure 3). When a profile ensemble is collected, water velocities relative to the glider are measured at a distance of about 10 m below the glider and turned into absolute water velocities by accounting for the absolute glider velocity using the bottom track velocity. Some 100 seconds later, assuming a nominal depth-rate of 10 cm s^{-1}, the glider reaches a depth at which it previously collected velocity data. On the assumption that vertical changes in currents are much greater than horizontal changes,

we estimate the water velocity at the current glider's depth from previously collected profile ensembles, and then compute the relative glider velocity by subtracting the glider absolute velocity (bottom track velocity) at this depth.

The drawback of this method is that in estimating the water velocity components at the glider's position, an average is constructed from profile ensembles taken 100 – 200 seconds earlier. No tendencies, or "future" profile ensemble data are taken into account. As an alternative, we also implemented a simple Kalman filter. A Kalman filter operates by propagating the mean and covariance of a state using a dynamic model, in an optimal way, given a time series of observations of the process (see e.g. Anderson and Moore 2005; Simon 2006). As dynamic model we choose a simple one: the acceleration of a current component (eastward, northward or up) at given depth is constant, with a model uncertainty of $\sigma^2 = 1 \times 10^{-16}$ m^2 s^{-4} to reflect the fact that the model is only approximate in describing the real system. The state vector consists of a velocity component at given depth, and the corresponding acceleration. This filter is run for each component and depth-bin separately, using measurements of the water velocity when they become available. The variance of the measurement noise is estimated at $\sigma^2 = 0.025^2$ m^2 s^{-2}, see also Section 4a. The filter is implemented as a forward-backward smoother, or so-called RTS filter after Rauch, Tung and Striebel who presented this filter in 1965, see Simon (2006). This filter is first run forward and then backward in time, making maximal use of available data.

In comparison with the Kalman filter, the averaging method is much simpler to implement and is also computationally considerably more efficient. The Kalman filter method, however, produces smoother, less noisy data, and has been used in the results reported in this work.

d. Incident water velocity from EMC measurements

The one-dimensional EMC sensor measures the velocity component along the principal axis of the glider (the ξ-axis, see Figure 1). Therefore, the incident water velocity derived from this sensor, U_{EMC}, relates to the actual measured velocity, $\hat{U}_{\mathrm{EMC}}$, as

$$U_{\mathrm{EMC}} = \frac{\hat{U}_{\mathrm{EMC}}}{\cos(\alpha)}. \tag{13}$$

Since α is not measured, values computed from the steady-state model, for example, can be used instead. These are generally small, so that $\cos(\alpha) = 1 + \mathscr{O}(\alpha^2)$. However, it is noted that due to local shear, the angle of attack may not always be small, leading to (13) being a lower bound estimate of the actual incident velocity.

During the processing of the EMC data it was found that the vertical water velocity computed from U_{EMC} and the glider's pitch angle was consistently larger in magnitude than the measured depth-rate. In contrast to the glider COMET, we have confidence in the pitch angles reported by glider IFM03, as they were nearly identical to the pitch angles reported by its Microrider sensor. Therefore, we applied a scaling factor to the velocities reported by the EMC so that the difference between the vertical velocity component and the depth-rate vanishes. Using the angle of attack estimated from the steady-state model (with lift angle and induced drag settings found for glider COMET, see next section), the factor was found to be equal to 0.93. A similar scaling factor was found by the Mircorider's manufacturer during tests with a SeaExplorer glider with a built-in Microrider with fitted EMC sensor, and an additionally mounted ADCP (R. Lueck, pers. comm.).

5. Glider flight model calibration and results

It is not possible to find optimal choices for both C_{D_0} and a when using only the depth-rate measurement as a model constraint; an additional velocity measurement with a significant orthogonal

(horizontal) component is required. In this section, we use measurements of the incident water velocity as additional model constraint to calibrate for the lift angle coefficient. This is done first for the DVL measurements and then for the EMC measurements.

Numerical values of drag and lift coefficients have a meaning only, if referenced to a known surface area S (see also equations (5) and (6). In this study, we follow the conventions used in aerodynamics, and use the surface area of the wings as reference area, giving $S = 0.1$ m2. Another choice for S could be the frontal area. To express drag and lift coefficients, referenced to the frontal area, the numerical values found in this study are to be multiplied by the ratio of wing area to frontal area.

In the subsections below, the value for the induced drag coefficient C_{D_1} used by the flight models, is preset to 10.5 rad^{-2}, anticipating the result presented at the end of this section where we also estimate the optimal value of C_{D_1}.

a. Lift angle coefficient

A simple approach is taken to estimate the optimal value of the lift angle coefficient a. To that end, an additional cost-function R_1 is defined as

$$R_1 = \frac{1}{N} \sum_{i=0}^{N-1} \left(U[i] - U_{\mathrm{DVL}}[i] \right)^2, \tag{14}$$

where $U_{\mathrm{DVL}}[i]$ is the incident water velocity derived from the DVL measurements with index i. The cost-function R_0 (10) is minimised for the parameter space $\{C_{\mathrm{D}_0}, m_{\mathrm{g}}\}$, for a range of preset values of a. Then, for each triplet $(C_{\mathrm{D}_0}, m_{\mathrm{g}}, a)$, the cost-function R_1 is evaluated.

Figure 4 summarises the results of these successive minimisation steps, using the steady-state model (solid lines) and the dynamic model (dashed lines), applied to data from a subinterval of four hours of data collected on 23 June 2017. The figure shows the optimal values for the parasite

drag coefficient and the mass (by minimising R_0) for a range of preset values of a. It is seen that the mass is independent of the value of the lift angle coefficient, but the drag coefficient is not. Moreover, the steady-state model estimates lower values for C_{D_0} than the dynamic model does, the explanation of which is left for Section 5c. The optimal value for a (for which the cost-function R_1 is minimal) is found to be $a \approx 7.4$ rad^{-1}, for both models, where also the mean difference between modelled and observed incident velocity is approximately zero.

We can now repeat the procedure to determine the glider flight model parameters C_{D_0}, m_g and a, but using the EMC derived incident velocity instead as the required non-vertical velocity component. The results are shown in Figure 5, and are found to be in line with the results obtained from the DVL data (cf. Figure 4). The data show a similar relationship between optimised lift and drag coefficient, and also the mass appears to be independent of the lift angle coefficient. For this glider (IFM03) an unbiased difference between measured and modelled incident velocities is found for $a = 7.5$ rad^{-1}, which is slightly higher than found for glider COMET.

In contrast to the DVL, the EMC provides continuous velocity data on both the up and down casts, so that the cost-function R_0 can be modified to include a non-vertical velocity component, yielding

$$R_2 = \frac{1}{N}\sum_{i=0}^{N-1} \kappa \left(U[i]\sin(\theta[i]+\alpha[i]) + \frac{\mathrm{d}h}{\mathrm{d}t}[i] \right)^2 + (1-\kappa)\left(U[i]-U^{\mathrm{EMC}}[i]\right)^2, \qquad (15)$$

where κ is a weighting coefficient, set to $\kappa = 1/2$, giving both velocity components equal importance assuming that the accuracy of their measurements is similar. The additional constraint allows for minimising R_2 for the parameter triplet C_{D_0}, m_g and a simultaneously, yielding $C_{D_0} = 0.136$, $m_g = 59.454$ kg and $a = 7.7$ rad^{-1}, indicated by the cross symbols in Figure 5.

The values for the lift angle coefficient, found for the gliders COMET (DVL) and IFM03 (EMC), are only slightly different. Figures 4 and 5 show, however, that a variation in a of 1 rad^{-1} would

lead to a bias in the incident velocity of approximately 6 mm s^{-1} and 3 mm s^{-1} for gliders COMET and IFM03, respectively. Given the uncertainties in the velocity measurements, we consider these findings to be consistent.

b. Induced drag coefficient

The induced drag coefficient C_{D_1} is another shape parameter, the setting of which may influence the results after calibrating the model for m_g, C_{D_0}, and a. From (9) it follows that the effect of the induced drag can be absorbed into the parasite drag coefficient if the glider is flown with pitch angles that are similar in magnitude for the up and down casts and (near) constant over time. In most cases this is how gliders are operated, and this second-order effect has little consequence on the model results. However, when operating gliders with microstructure sensors, the pitch battery position is usually fixed to avoid vibrations that can interfere with shear probe measurements during the moving of the pitch battery. As a consequence, especially for deep glider profiles, the pitch angle may vary substantially due to changes in the in-situ water density and compression of the hull, so that changes in flight due to the induced drag depend on the depth. The compressibility of the hull also causes the flight to change with depth, and hence it is difficult to distinguish between both effects.

At the end of the glider experiment in dataset II, the pitch settings of the glider COMET were varied. Over the course of a day, the target pitch was changed to the following three values $\theta_t = 16°, 19°, 27°$, where the absolute values of the target pitch angles θ_t were the same for up and down casts. Using a lift angle coefficient $a = 7.5$ rad^{-1} as found previously, the glider flight model was calibrated for the mass and total drag coefficient, $C_D = C_{D_0} + \alpha^2 C_{D_1}$, for the three subsets, each having a narrow range of pitch angles, see Figure 6, right-hand side panel. The optimisation routine yields for each pitch band a different value for C_D. Since the angle of attack

can be assumed more or less constant within each pitch band, C_D can be plotted as function of the corresponding angle of attack, see the blue dots in Figure 6, left panel. As the induced drag effect is proportional to the angle of attack squared, a parabola is fitted to the data, yielding $C_{D_0} = 0.147$ and $C_{D_1} = 10.5$ rad^{-2}. The value found for the induced drag coefficient is significantly higher than the one estimated by Merckelbach et al. (2010), who suggested a total value for the induced drag of about 3 rad^{-2}. The discrepancy is most likely to be due to the protruding features that the glider has, such as the tail fin, the CTD, and most importantly the Microrider package, which was not considered by Merckelbach et al. (2010).

Like the parasite drag coefficient, the induced drag coefficient is likely to change when the vehicle gets biofouled. The value quoted here, was determined for a glider without noticeable biofouling. But, as argued before, the effect due to the induced drag is of second-order importance, and some change in the induced drag coefficient due to biofouling is likely to be insignificant.

c. Results

After calibrating the flight model for mass, parasite and induced drag coefficients, and lift angle coefficients above, we use subsets of the data and solve both the steady-state and dynamic model to yield time series of incident water velocities. By comparing the time series with measurements we can assess the model performance.

First we compare the model results with measurements obtained with the DVL for two subsets of about four and nine hours of data, respectively. Measurements and model results are shown in Figure 7 for two intervals comprising four full yos down to 40 m of water depth spanning about 30 minutes on 23 June 2017 (top panels) and on 24 June 2017 (bottom panels), respectively. The incident water velocity computed from the DVL measurements are available only for water depths in excess of about 10 m and during down casts. The DVL measurements (blue curves, left-

hand side panels) show that the glider quickly gains speed when starting the down cast and then gradually slows down as the it gets deeper. This deceleration is also reproduced in the incident water velocities computed by the steady-state model (orange) and the dynamic model (red). The reason for this is that the in-situ density increases with depth, reducing the glider's weight in water with depth. The deceleration observed during the up casts are due to the same reason. In a situation like this, when the glider decelerates during most of the up and down casts, the dynamic model adjusts to the observed change in density with a response time of the order of a minute, whereas the steady-state model adjusts instantly. As a result, the steady-state model computes lower speeds through water than the dynamic model would for the same flight model parameter setting. So, if both models are calibrated separately, the steady-state model has a lower drag coefficient, compensating the lower speed through water, as we observed in Section 5 (Figure 4).

For depths greater than about 12-15 m, down to the dive-to-climb turning points, the steady-state and dynamic model appear to yield identical results, indicating that, as expected, for most of each cast the glider's dynamical behaviour can be considered steady-state. Only for short periods after changing cast direction, the dynamic model shows a gradual response to the sudden changes in forcing, where the steady-state model predicts unrealistic overshoots. Discrepancies between steady-state and dynamic model near the dive-to-climb turning points are present, but not clearly visible in this figure. The model performance during rapid changes when changing from down cast to up cast are discussed in detail below.

Restricted to the steady-state region, both models compare favourably with the measurements. In particular for the data from 23 June (top panel), the model estimates are typically within 1-2 cm s^{-1} of the observations. For 24 June, however, the measurements exhibit more variability with discrepancies between observations and model estimates amounting up to about 4 cm s^{-1}. The difference in the degree of agreement between model and observations is most likely related to

environmental factors. Indeed, the variance of the water velocity relative to the bed in the flight direction, computed as an average per profile for the profiles shown, is more than 15 times larger for the profiles of 24 June than those of 23 June. Because the lift and drag force parameterisations do not account for the presence of shear, it seems likely that the increased levels of shear on 24 June contribute to the increased variability in observed incident water velocity.

A subset of data comprising close to two days of data of the glider IFM03 is processed in a similar way. A selection of 2 full yo cycles is shown in Figure 8 comparing the measurements with the modelled results from the dynamic model. Since for most of the 800 m dives, the steady-state and dynamic models produce identical results, the data of the former are not displayed. Also, note that in comparison with the glider COMET, the time scale is condensed by a factor of 20 due to the deeper dives.

The incident water velocity measured by the EMC agrees, on average, well with the results of the dynamic model. However, some variability captured by the EMC sensor, is not represented by the dynamic model. Differences between modelled and observed velocities amount to up to about 4 cm s^{-1} and have time scales of minutes. Like the previous dataset, most of the discrepancies between measurements and modelled results are attributed to the local variability in the flow. Another recurrent feature is that at the beginning of the first dive (and for this glider all dives as all dive cycles within this time interval comprised one full yo only), the glider accelerates slower than the model estimates. This is most likely due to trapped air bubbles, as discussed in Section 6c.

6. Discussion

a. Implications for turbulent microstructure measurement

Two key findings from the above analysis are (i) the values of calibrated drag and lift parameters are similar between two different gliders applied in different conditions, and (ii) that the time series show good agreement between the observed and modelled glider speed through water, U. A question that naturally arises is what errors a (calibrated) glider flight model then produces in U, and what implications this has for estimates of the dissipation rate from temperature and shear microstructure. These errors add to the uncertainty of the dissipation rate measurements over that for standard free-fall profilers, where the speed along the sensors is estimated from the pressure rate of change. Although not rigorously derived, the uncertainties of free-fall profilers are generally estimated at a factor of approximately two (Dewey and Crawford 1988; Moum et al. 1995).

To estimate the errors produced from deviations in the measured and modelled glider speeds, we first note the scaling of the dissipation rate, ε, with the flow speed past the sensors, U. For ε measured with airfoil shear probes,

$$\varepsilon = \frac{15}{2}\nu\overline{\left(\frac{\partial v}{\partial x}\right)^2}, \tag{16}$$

where x represents distance in the glider path direction, v denotes across-path velocity fluctuations, ν is the kinematic viscosity, and the bar denotes a mean. The probe returns a signal, $E(t)$, that is proportional to Uv (the lift force on the probe), so we can express the across path velocities as $v \propto E/U$. Spatial gradients of v are then found using Taylor's frozen turbulence hypothesis, whereby

$$\frac{\partial v}{\partial x} = \frac{1}{U}\frac{\partial v}{\partial t} \propto \frac{1}{U^2}\frac{\partial E}{\partial t}. \tag{17}$$

Therefore,

$$\varepsilon \propto \frac{1}{U^4}\overline{\left(\frac{\partial E}{\partial t}\right)^2}, \tag{18}$$

showing that ε scales with the fourth power of the flow speed past the sensors, and will thus be sensitive to errors in its estimation. Note that if ε is measured by using microstructure temperature sensors (Gregg 1999; Ruddick et al. 2000) then $\varepsilon \propto U^{-2}$ due to the lack of U dependence arising from the lift force in the case of shear probes.

Errors in the estimation of ε arising from deviations between the glider flight model and the true speed through water, will therefore appear through the factor $(U_{\mathrm{meas}}/U_{\mathrm{dyn}})^n$, where $n = \{2,4\}$ for measurements from microstructure temperature sensors, and shear probes, respectively, and the U ratio corresponds to the measured speed to that obtained from the dynamic model. These factors are computed as profile averages (indicated by angled braces) in Figure 9 from the DVL data sets. It shows averages as solid lines with the shaded area indicating twice the standard deviation in the data for both DVL data sets. Depths shallower than 12 m are not shown, since no reliable DVL data can be collected (see also Section 4c). Although some bias towards positive or negative differences, amounting to close to 1 cm s^{-1} exists, the bias is not systematic, as it is different for two consecutive deployments. When multiple deployments are considered, there is negligible bias in the difference between mean measured and modelled speeds.

The histograms in Figure 9 show that 90% of the errors expected in dissipation rate estimates due to modelled glider speeds are within a factor of 0.67–1.43 for shear probe measurements ($n = 4$), and within 0.82–1.26 for temperature microstructure ($n = 2$). These errors should be compared to the factor of 2 uncertainty normally associated with dissipation rate measurements from vertical profilers (Dewey and Crawford 1988; Moum et al. 1995). In addition, it is not clear how much of this difference between modelled and measured speeds can be attributed to the need to use

DVL measurements that are not coincident in time and space with the glider position, and require averaging to reduce measurement noise.

An advantage the EMC sensor has over the DVL is that it measures velocities co-located in time and space with the glider flight model. As long as the instantaneous angle of attack remains small, the measured quantity represents the glider speed through water, an assumption we have made in the analysis. The same profile averaged quantities as in Figure 9, but now for the EMC sensor, are shown in Figure 10. For depths deeper than 150 m, we also find unbiased results, with error ratios that have a smaller spread than for the DVL [i.e., 90% of the data lie in the ranges of $0.83 < \langle (U_{\mathrm{EMC}}/U_{\mathrm{dyn}})^4 < 1.20$ and $0.91 < \langle (U_{\mathrm{EMC}}/U_{\mathrm{dyn}})^2 < 1.09$]. The velocity measurements made by the EMC sensor have a standard deviation that is about an order of magnitude smaller than the readings from the DVL (Section 4a), so that this suggests that a fraction of the spread of the data observed for the DVL (and possibly also for the EMC) could be due to uncertainty in the measurements.

If the steady-state model were applied to the present data, but using a lift angle coefficient of 6.1 rad^{-1} (Merckelbach et al. 2010), then the bias in the difference between measured and modelled incident velocities would be 1.3 and 0.5 cm s^{-1} for datasets I (Figure 4) and III (Figure 5), respectively. The associated biases in the estimates for the dissipation rate applied to dataset I (dataset III) would an underestimation of a factor of 1.10 (1.05) and 1.20 (1.07) for estimates from temperature microstructure sensors and shear probes, respectively. The bias sensitivity to the error in the specification of the lift angle coefficient depends on steepness of the dives and climbs, where smaller pitch angles cause larger biases.

b. Dynamic versus steady state flight

Thus far, we have concluded that for most of the dive and climb, the glider can be considered in a regime of steady-state. This is demonstrated by the close agreements between steady-state and dynamic model results throughout most of the flight (Figures 7, 8). Since implementing the dynamic model is computationally more expensive, this brings up the question of whether the extra effort is needed. The dynamic model handles situations better which involve sudden and significant changes in the forcing. Examples of such instances are when pitch battery positions change during flight, when the glider experiences a strong pycnocline, or during the transit from down cast to up cast. Standard practice is to discard microstructure data when steady-state conditions are not met. Employing a dynamic model however, may somewhat relax this restriction.

To examine this in more detail we focus on a transition from dive to climb. Figure 11 is a zoom-in of such an event of the time series from Figure 8, showing the speed through water during the last segment of a down cast, its transition to the up cast (marked by the gray box) and a full up cast, until the glider reached the surface. Most of the flight is in the steady-state regime as the results of the steady-state model (orange curve) and dynamic model (red curve) are indiscernible in this regime. During the transition from down cast to up cast (gray box, and highlighted in the in-set), the model results diverge and the flight is not steady-state. As soon as the glider initiates the transition, the pitch battery is set to its position for the upcast, suddenly increasing the pitch angle (green curve in inset). Concurrently, the measured speed through water is seen to decrease. After reaching a minimum velocity of 12 cm s^{-1}, the glider gradually accelerates, until the flight becomes steady-state again. The steady-state model computes false behaviour during the transition. The dynamic model, however, does reproduce the dip in speed.

c. Flight model error sources

Although errors in the velocity measurements lead to discrepancies between measured and modelled incident velocities, some of these discrepancies can be related to the model failing to capture all aspects of the glider flight. For water depths less than 150 m, discrepancies between observed and modelled velocities are very clearly present in the dataset of glider IFM03 (Figure 10). It is unlikely that these discrepancies can be related to inaccurate velocity measurements. It is, however, a known issue for Slocum gliders with an oil-based displacement pump, such as the glider IFM03, that air can diffuse into the oil system. Air bubbles in the oil system will lead to inaccurate reporting of the actual glider volume change, causing the flight model to compute erroneous buoyancy forces, and as a result erroneous flight velocities. Because there is currently no way to measure how much air is present, and where it resides, this aspect is not included in the flight model. The effect of air bubbles can be identified by comparing the computed vertical glider velocities with the observed depth rate; if calibrated for deep dives, the presence of air bubbles manifests itself as a bias in the vertical velocity difference during the shallower part of the dives.

A further assumption underlying both the steady-state and dynamic flight models is that the ocean currents are steady and free of shear. The consequence is that in the presence of, for example, vertical shear and internal waves with short periods, the inertia of the glider can cause the instantaneous incident velocity to be significantly different from the modelled incident velocity, introducing errors in the drag and lift forces computed by the model. Unfortunately, this issue is not remedied by the dynamic model developed herein, despite having the inertial terms included. This is because the model cannot discern between the glider velocity in an inertial frame, the time derivative of which equals the acceleration, and the incident water velocity (relative to the glider), which is used in the parameterisations of the lift and drag forces. The results shown in Figures 7,

and 8 indicate that the discrepancies observed between the measured incident velocities and the dynamic model results occur on time scales of the order of 1–10 minutes, and are likely caused by the model failing to capture the effects due to an unsteady ocean.

The present measurements suggest that the steady ocean assumption introduces errors in the estimates of the dissipation rate that are within acceptable levels given the current uncertainties in microstructure estimates. This may not be true anymore for more dynamic environments than those encountered in this study, so that in those conditions measuring the dissipation rate with an acceptable accuracy may still require direct measurements of the glider flight.

7. Conclusions

This study is the first to use measurements of in-situ glider flight to test, calibrate, and extend a glider flight model. Our principal motivation is to quantify and reduce uncertainties in the use of flight models for turbulent microstructure studies. Calibration of the steady-state model of Merckelbach et al. (2010) resulted in changes in the lift angle coefficient to $a = 7.5$ rad^{-1}, as well as the induced drag coefficient $C_{D_1} = 10.5$ rad^{-1}. This change in the value of the lift angle coefficient from that reported in Merckelbach et al. (2010) results in a reduction of the difference between measured and modelled incident water velocity of about 0.5–1.3 cm s^{-1}.

Measurements of in-situ glider flight allow us to quantify errors in dissipation rate calculations associated with errors in the incident water velocity predicted by the flight model. Using velocities from the EMC as a baseline, we found that 90% of the estimates of dissipation rate based on the calibrated flight model are within a factor of 1.1 and 1.2 for measurements derived from microstructure temperature sensors and shear probes, respectively. The uncalibrated model would produce a bias of factors of 1.05–1.10 and 1.07–1.20, for temperature and shear microstructure, respectively. The uncertainty in dissipation rate estimates can be attributed to the local variabil-

ity in the flow, which is not accounted for in the flight model, as well as possible noise from the velocity measurement itself. When using water velocities measured with the DVL, for which the estimates are more prone to instrument noise, the factors are slightly larger, namely 1.2 and 1.4, respectively.

To better represent the hydrodynamics we have extended the steady-state glider flight model of Merckelbach et al. (2010) to a dynamic model by including the inertial and added mass terms. A comparison of the two models found that the flight is largely well-described by the steady-state model, and that only when conditions change rapidly, such as during dive-climb transitions, does the steady-state model fail, whereas the dynamic model predicts the incident water velocity reasonably well.

Acknowledgments. We are grateful to Rolf Lueck (Rockland Scientific) for the useful discussion on the interpretation of the velocities measured with the electromagnetic current meter. We also thank David Pheifer (True North Technologies) for sharing his expertise on how to correct the attitude data of glider COMET. The bathymetry used in this work were provided by GEBCO (www.gebco.net). This paper is a contribution to the projects M6 and T2 of the Collaborative Research Centre TRR 181 "Energy Transfer in Atmosphere and Ocean", and the project B6 of the Collaborative Research Centre SFB 754 "Climate - Biogeochemistry Interactions in the Tropical Ocean", all funded by the German Research Foundation (Deutsche Forschungsgemeinschaft). Part of the measurements (dataset I) took place during the Expedition Clockwork Ocean, which was partially supported by the Helmholtz-Zentrum Geesthacht as part of its PACES II programme. We thank the captain and crew of the R/V Elisabeth Mann Borgese for the excellent technical support and express our appreciation for the constructive comments and suggestions by two anonymous reviewers.

The data used in this manuscript are available under https://doi.org/10.5281/zenodo.2270123.

References

Anderson, B. D., and J. D. Moore, 2005: *Optimal Filtering*. Dover Publications.

Davis, R., C. Eriksen, and C. Jones, 2002: Autonomous buoyancy-driven underwater gliders. *Technol. Appl. Auton. Underw. Veh.*, Taylor and Francis, Ed., London, 324, doi:10.1201/9780203522301.ch3.

Dewey, R., and W. Crawford, 1988: Bottom stress estimates from vertical dissipation rate profiles on the continental shelf. *J. Phys. Oceanogr.*, **18**, 1167–1177.

Fer, I., A. K. Peterson, and J. E. Ullgren, 2014: Microstructure measurements from and underwater glider in the turbulent Faroe Bank channel overflow. *J. Atmos. Ocean. Technol.*, **31**, 1128–1150.

Garau, B., S. Ruiz, W. G. Zhang, A. Pascual, E. Heslop, J. Kerfoot, and J. Tintoré, 2011: Thermal lag correction on slocum ctd glider data. *Journal of Atmospheric and Oceanic Technology*, **28**.

Gregg, M., 1999: Uncertainties and limitations in measuring ε and χ_T. *J. Atmos. Oceanic Technol.*, **16**, 1483–1490.

Imlay, F., 1961: The complete expressions for added mass of a rigid body moving in an ideal fluid. Tech. Rep. 1528, David Taylor Model Basin.

Merckelbach, L., 2018: Glider flight v1.0.0. URL https://github.com/smerckel/gliderflight, doi:10.5281/zenodo.2222694.

Merckelbach, L., D. Smeed, and G. Griffiths, 2010: Vertical velocities from underwater gliders. *Journal of Oceanic and Atmospheric Technology*, **27**, 547–563.

607 Moum, J., M. Gregg, R. Lien, and M. Carr, 1995: Comparison of turbulence kinetic energy dissi-
608 pation rate estimates from two ocean microstructure profilers. *J. Atmos. Oceanic Technol.*, **12**,
609 346–366.

610 Newman, J., 1977: *Marine hydrodynamics*. MIT Press.

611 Palmer, M., G. Stephenson, M. Inall, C. Balfour, A. Düsterhus, and J. Green, 2015: Turbulence
612 and mixing by internal waves in the Celtic Sea determined from ocean glider microstructure
613 measurements. *J. Marine Sys.*, **144**, 57–69, doi:10.1016/j.marsys.2014.11.005.

614 Peterson, A. K., and I. Fer, 2014: Dissipation measurements using temperature microstructure
615 from an underwater glider. *Meth. Oceanogr.*, **10**, 44–69, doi:10.1016/j.mio.2014.05.002.

616 Ruddick, B., A. Anis, and K. Thompson, 2000: Maximum likelihood spectral fitting: the Batchelor
617 spectrum. *J. Atmos. Oceanic Technol.*, **17**, 1541–1555.

618 Rudnick, D., 2016: Ocean research enabled by underwater gliders. *Ann. Rev. Mar. Sci.*, **8 (1)**,
619 519–541, doi:10.1146/annurev-marine-122414-033913.

620 Scheifele, B., S. Waterman, L. Merckelbach, and J. Carpenter, 2018: Measuring the dissipation
621 rate of turbulent kinetic energy in strongly stratified, low-energy environments: A case study
622 from the Arctic Ocean. *J. Geophys. Res. Oceans*, **123**, doi:10.1029/2017JC013731.

623 Schultze, L., L. Merckelbach, and J. Carpenter, 2017: Turbulence and mixing in a shallow
624 stratified shelf sea from underwater gliders. *J. Geophys. Res. Oceans*, **122**, doi:10.1002/
625 2017JC012872.

626 Simon, D., 2006: *Optimal State Estimation*. Wiley and Sons, 526 pp.

627 St. Laurent, L., and S. Merrifield, 2017: Measurements of near-surface turbulence and mixing
628 from autonomous ocean gliders. *Oceanogr.*, **30**, 116–125, doi:10.5670/oceanog.2017.231.

TeledyneRDI, 2017: Rdi explorer dvl datasheet. Retreived from http://www.teledynemarine.com/Lists/Downloads/explorer_datasheet_hr.pdf at 30 November 2018.

Todd, R., D. Rudnick, J. Sherman, W. Owens, and L. George, 2017: Absolute velocity estimates from autonomous underwater gliders equipped with doppler current profilers. *Journal of Atmospheric and Oceanic Technology*, **34 (2)**, 309–330.

Wolk, F., R. Lueck, and L. St. Laurent, 2009: Turbulence measurements from a glider. *13th Workshop on Physical Processes in Natural Waters Proceedings*, 1-11.

LIST OF TABLES

Dataset	Glider	Velocity Sensor	Region	Start	End
I	COMET	DVL	Baltic Sea (SW)	2016 June 20	2016 June 26
II	COMET	n.a.	Baltic Sea (Central)	2017 October 19	2017 October 28
III	IFM03	EMC	Peru	2017 April 29	2017 May 23

TABLE 1. Dates and regions of the datasets used.

LIST OF FIGURES

683 the corresponding colour indicates the spread in the data, computed from twice the standard
684 deviation. The histograms above the profiles show the distribution of the corresponding
685 observations. The data in purple respresent a 4-hour deployment period (23 June 2017 17:51
686 – 21:58) whereas the data in blue represent a 9-hour deployment period (24 June 2017 17:54
687 – 25 2017 June 3:04). The dashed lines represent the 5 and 95 percentiles, computed over
688 both datasets. 44

689 **Fig. 10.** A comparison of the glider speed through water, computed from EMC measurements and
690 from the dynamic flight model. The panels show profile averages of difference between
691 the velocities (left), the squared ratio of the velocities (middle) and the ratio of the velocity
692 raised to the fourth power (right) as solid lines. The shaded region in the corresponding
693 colour indicates the spread in the data, computed from twice the standard deviation. The
694 down casts and up casts are drawn in blue and red, respectively. The histograms above the
695 profiles show the distribution of the corresponding observations. The dashed lines represent
696 the 5 and 95 percentiles, computed over both the down and up casts combined. The data
697 encompasses a 45-hour period (12 May 2017 00:20 – 13 May 2017 21:13). 45

698 **Fig. 11.** A section of a time series showing the speed through water as measured by the EMC (blue
699 curve), the steady-state model (orange), and a dynamic glider flight model (red). The inset
700 is a zoom of a deep transition from dive to climb. 46

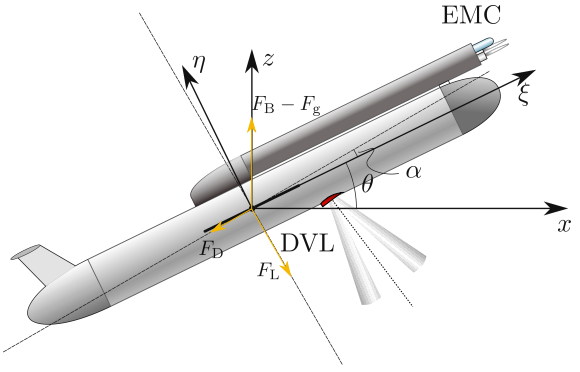

FIG. 1. Schematic representation of a glider, defining an orthogonal coordinate system with horizontal and vertical axes (x, z), and an orthogonal glider referenced coordinate system (ξ, η). The latter originates from the former after a rotation of the pitch angle θ. The glider path, indicated by the dashed line, makes a small angle, equal to the angle of attack α, with the glider's principal axis, which coincides with the ξ-axis. The forces due to drag, lift and net buoyancy are drawn by the yellow vectors. The positions of the electromagnetic current sensor (EMC) and the Doppler Velocity Log (DVL) are drawn in blue and red, respectively. The DVL is mounted such that the principal axis of the DVL (dashed) makes an 11° angle with the η-axis.

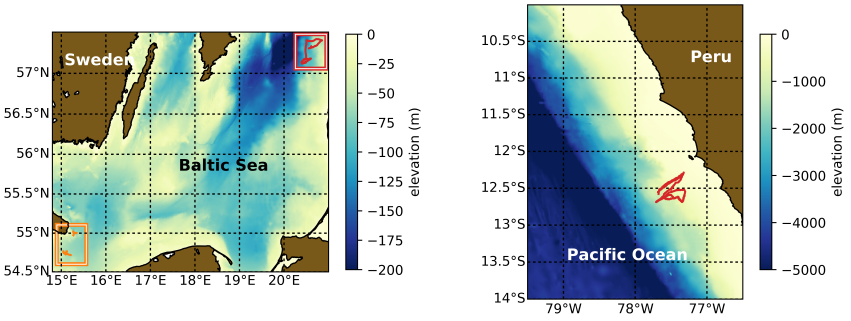

FIG. 2. Maps of where glider missions were carried out. Left panel: the Baltic Sea, where two missions were carried out with glider COMET, yielding dataset I (2016, inside orange box) and Data set II (2017, inside red box). Right panel: coastal shelf of Peru (Pacific Ocean), yielding dataset III (2017).

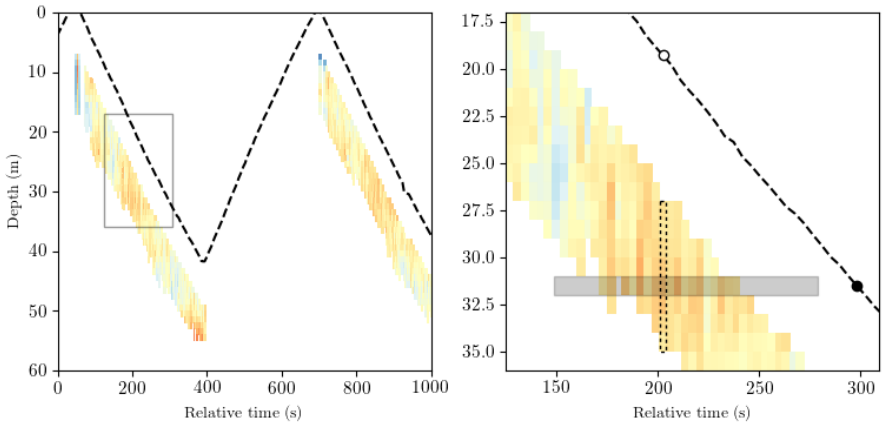

FIG. 3. Construction of water current profiles, expressed in a geographic Cartesian reference frame, as measured by a profiling glider. The dashed line represents the glider's path. Current profiles are measured during the down cast only (left panel). The right-hand side panel is a zoom of the rectangle in the left-hand side panel. At $t = 200$ s, the glider (indicated by the open circle) collects an absolute velocity profile, of which usable data are delineated by the dashed rectangle. Some 100 seconds later, the absolute velocity at the depth of the glider (solid circle) can be estimated from previous measurements (marked shaded rectangle). Subtracting the bottom track velocity from the thus estimated absolute velocity yields the relative velocity.

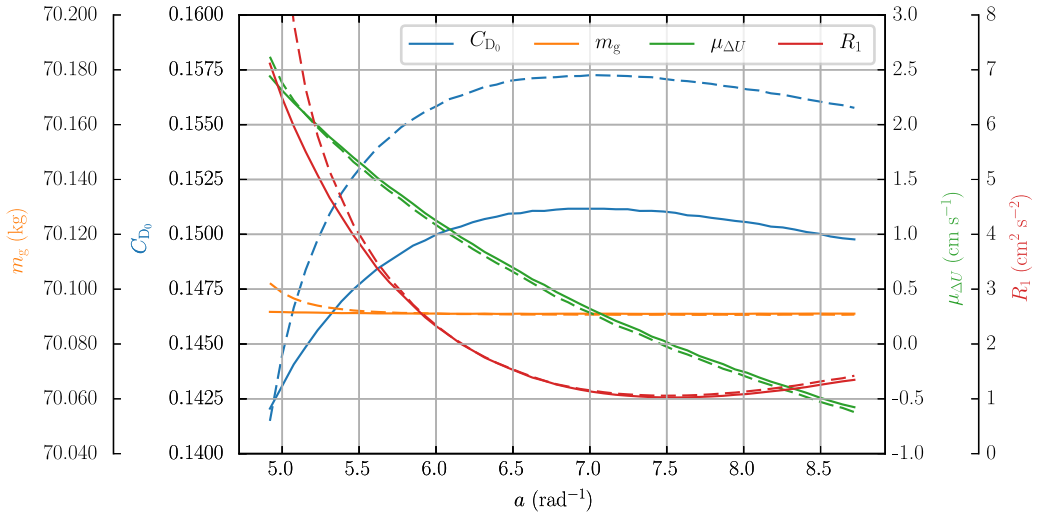

FIG. 4. Dependency of the calibration parameters m_g and C_{D_0} on the lift angle coefficient a (left ordinate axes), and corresponding mean and standard deviations of the difference between the modelled and measured (DVL) incident velocity, as well as the cost-function R_1 (right ordinate axes). Results are shown for the steady-state model (solid lines) and the dynamic model (dashed lines). The mean of the incident velocity difference is denoted by $\mu_{\Delta U}$.

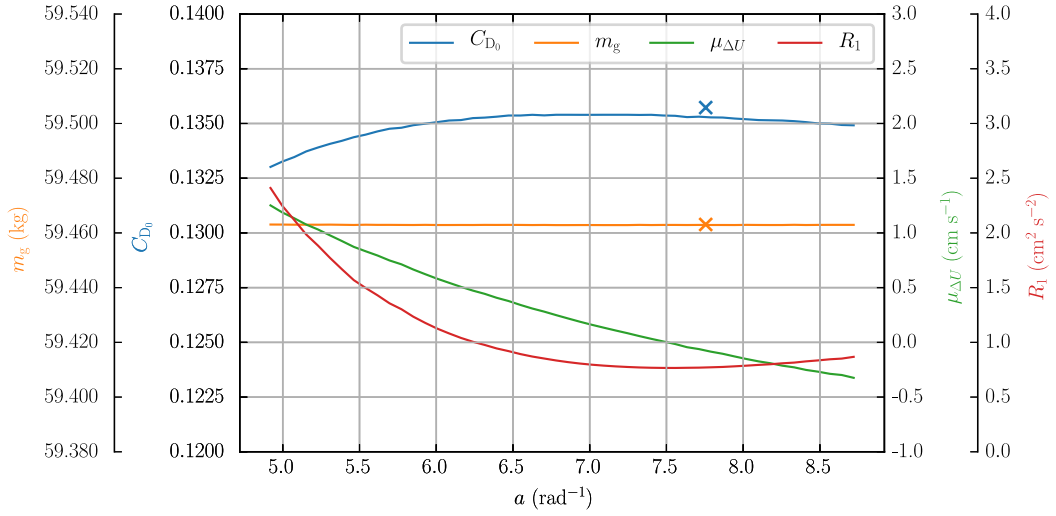

723 FIG. 5. Dependency of the calibration parameters m_g and C_{D_0} on the lift angle coefficient a (left ordinate
724 axes), and corresponding mean and standard deviations of the difference between the modelled and measured
725 (EMC) incident velocity, as well as the cost-function R_1 (right ordinate axes). The cross symbols indicate the
726 results of a minimisation of cost-function R_2.

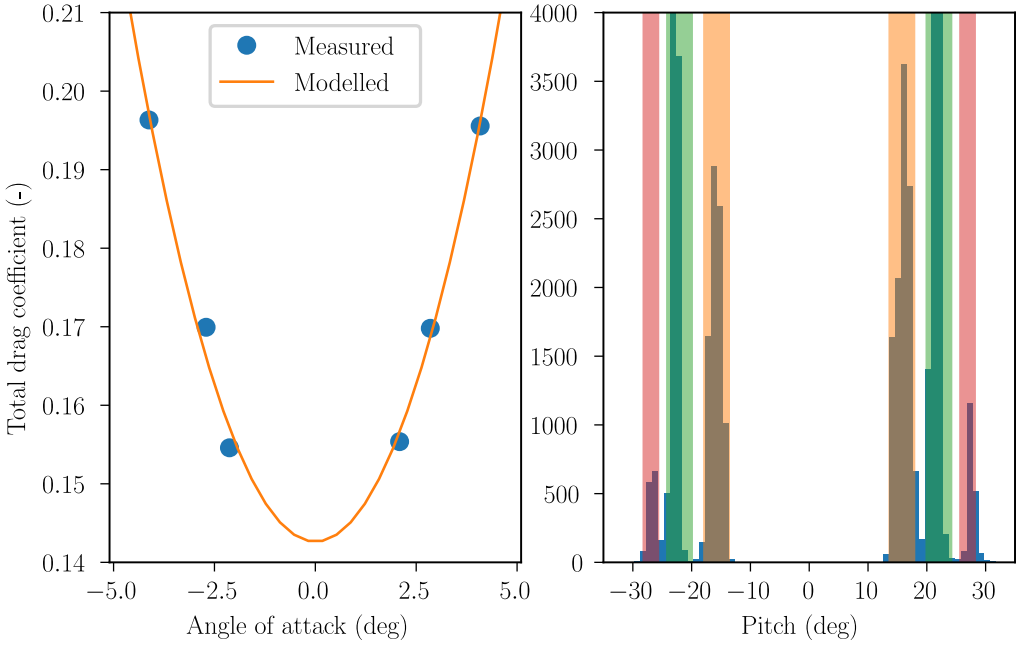

FIG. 6. Left panel: total drag as a function of the angle of attack. Right panel: a histogram of realised pitch angles during a number of dives (dataset II). The coloured bars indicate the three time subintervals, selected from this dataset: gentle dives (orange), nominal dives (green) and steep dives (red).

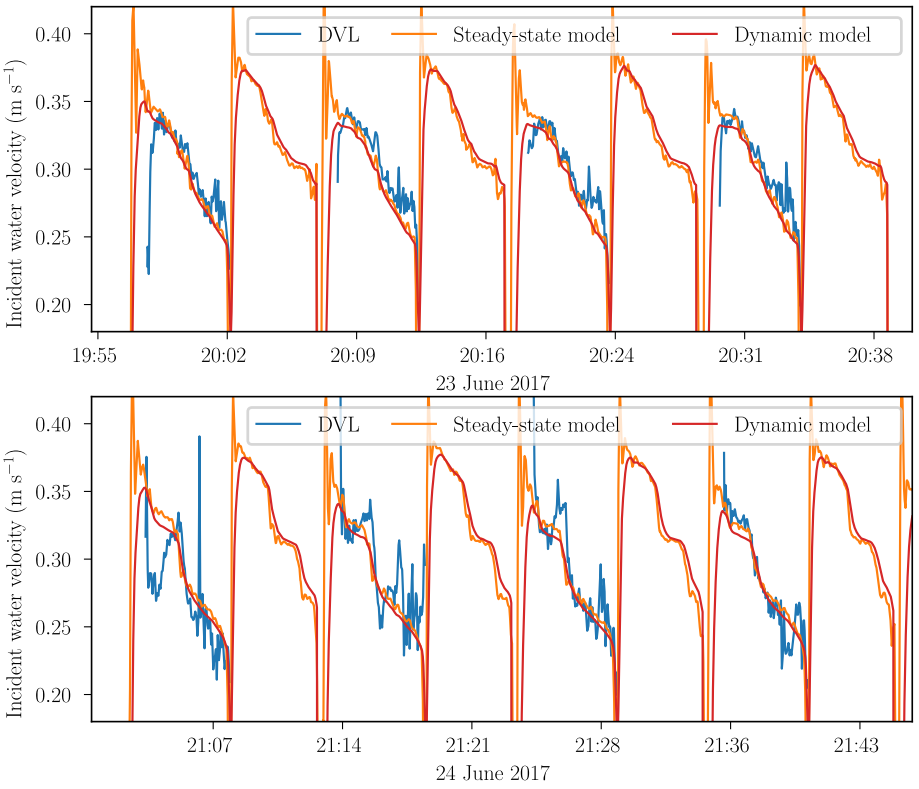

730 FIG. 7. A comparison of incident water velocities measured with the DVL and computed by the calibrated
731 steady-state model and dynamic model for two half-hour intervals.

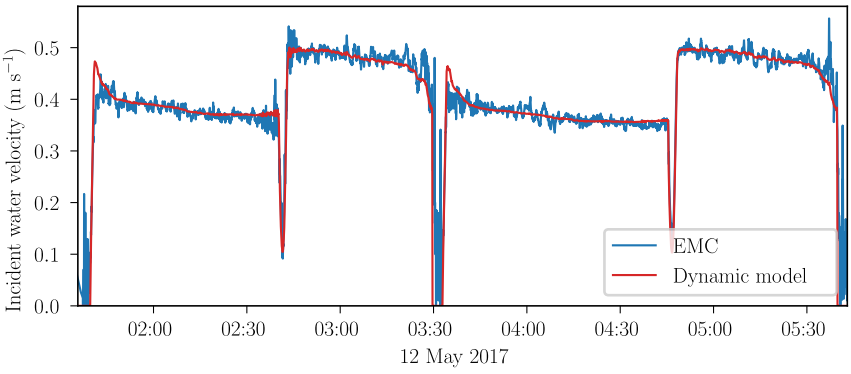

732 FIG. 8. A comparison of incident water velocities measured with the EMC (blue) and computed by the
733 calibrated dynamic model (red).

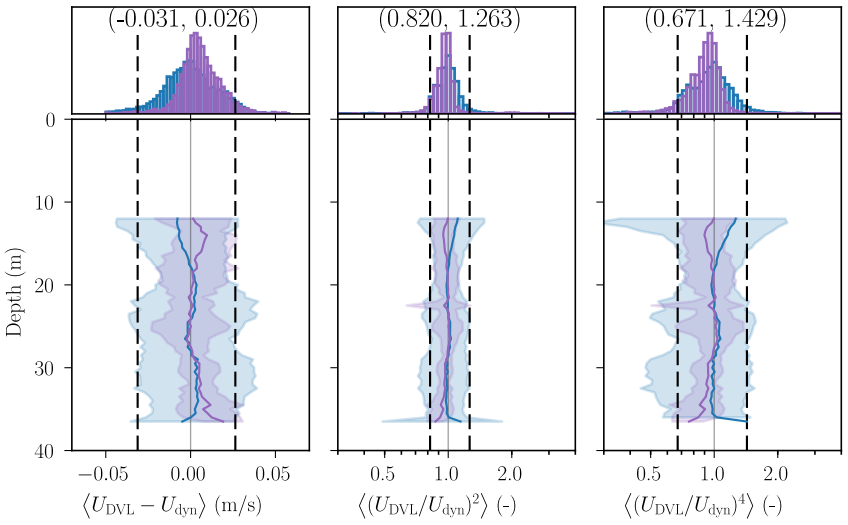

734 FIG. 9. A comparison of the glider speed through water, computed from DVL measurements and from the
735 dynamic flight model (down casts only). The panels show profile averages of difference between the velocities
736 (left), the squared ratio of the velocities (middle) and the ratio of the velocity raised to the fourth power (right)
737 as solid lines. The shaded region in the corresponding colour indicates the spread in the data, computed from
738 twice the standard deviation. The histograms above the profiles show the distribution of the corresponding
739 observations. The data in purple respresent a 4-hour deployment period (23 June 2017 17:51 – 21:58) whereas
740 the data in blue represent a 9-hour deployment period (24 June 2017 17:54 – 25 2017 June 3:04). The dashed
741 lines represent the 5 and 95 percentiles, computed over both datasets.

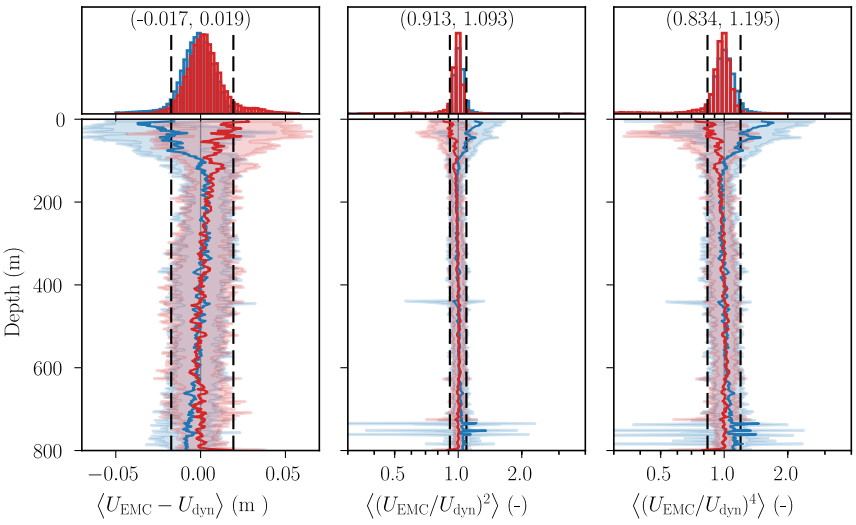

FIG. 10. A comparison of the glider speed through water, computed from EMC measurements and from the dynamic flight model. The panels show profile averages of difference between the velocities (left), the squared ratio of the velocities (middle) and the ratio of the velocity raised to the fourth power (right) as solid lines. The shaded region in the corresponding colour indicates the spread in the data, computed from twice the standard deviation. The down casts and up casts are drawn in blue and red, respectively. The histograms above the profiles show the distribution of the corresponding observations. The dashed lines represent the 5 and 95 percentiles, computed over both the down and up casts combined. The data encompasses a 45-hour period (12 May 2017 00:20 – 13 May 2017 21:13).

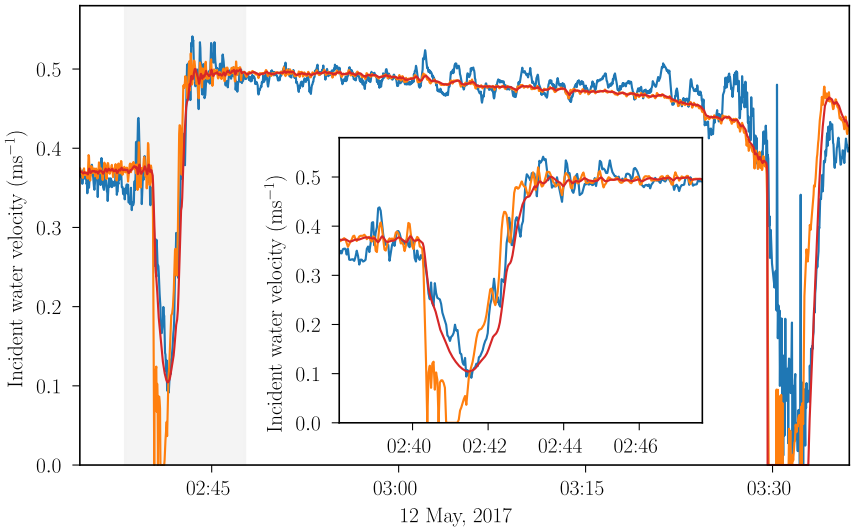

FIG. 11. A section of a time series showing the speed through water as measured by the EMC (blue curve), the steady-state model (orange), and a dynamic glider flight model (red). The inset is a zoom of a deep transition from dive to climb.